Plasmonic Nanoparticle Simulations and Inverse Design Using Machine Learning

5 authors, including:

Jing He
Shanghai Jiao Tong University
6 PUBLICATIONS **15** CITATIONS

Qiang Wang
Shanghai Jiao Tong University
1 PUBLICATION **1** CITATION

Jian Ye
Shanghai Jiao Tong University
83 PUBLICATIONS **2,008** CITATIONS

Some of the authors of this publication are also working on these related projects:

Plasmonic enhanced mass spectrometry View project

Asymmetric plasmonic nanostructures View project

Nanoscale

Accepted Manuscript

Volume 10
Number 4
28 January 2018
Pages 1549-2172

Nanoscale

rsc.li/nanoscale

ISSN 2040-3372

ROYAL SOCIETY
OF CHEMISTRY

PAPER
Shuping Xu, Chongyang Liang et al.
Organelle-targeting surface-enhanced Raman scattering
(SERS) nanosensors for subcellular pH sensing

NCNST

ROYAL SOCIETY
OF CHEMISTRY

rsc.li/nanoscale

Plasmonic Nanoparticle Simulations and Inverse Design Using Machine Learning

Jing He,[†,Δ] Chang He, [†,Δ] Chao Zheng,[†] Qian Wang,[#] and Jian Ye[*,†,‡,#]

[†]State Key Laboratory of Oncogenes and Related Genes, School of Biomedical Engineering, Shanghai Jiao Tong University, Shanghai, P. R. China

[‡]Shanghai Key Laboratory of Gynecologic Oncology, Ren Ji Hospital, School of Medicine, Shanghai Jiao Tong University, Shanghai, P. R. China

[#]Shanghai Med-X Engineering Research Center, School of Biomedical Engineering, Shanghai Jiao Tong University, Shanghai, P. R. China

RECEIVED DATE (to be automatically inserted after your manuscript is accepted if required according to the journal that you are submitting your paper to)

[*]To whom correspondence should be addressed. E-mail: yejian78@sjtu.edu.cn;

[Δ]These authors contributed equally to this work.

ABSTRACT

Collective oscillation of quasi-free electrons on the surface of metallic plasmonic nanoparticles (NPs) in the regime from ultraviolet to near-infrared (NIR) induces strong electromagnetic enhancement around the NPs, which leads to numerous important applications. These interesting far- and near-field optical characteristics of the plasmonic NPs can be typically obtained from numerical simulations for theoretical guidance of NP design. However, traditional numerical simulations encounter irreconcilable conflicts between the accuracy and speed due to high demand of computing power. In this work, we utilized the machine learning method, specifically deep neural network (DNN), to establish mappings between the far-field spectra/near-field distribution and dimensional parameters of three types of plasmonic NPs including nanosphere, nanorod, and dimer. After training process, both the forward prediction of far-field optical properties and the inverse prediction of on-demand NP's dimensional parameters can be accomplished accurately and efficiently by DNN. More importantly, we first time achieve ultrafast and accurate prediction of two-dimensional on-resonance electromagnetic enhancement distributions around NPs by greatly reducing the amount of electromagnetic data via screening and resampling methods. These near-field predictions can be realized typically in less than 10^{-2} second on a laptop, which is 6 orders faster than typical numerical simulations implemented on a server. Therefore, we demonstrate that the DNN is an ultrafast, highly efficient, and computing resource-saving tool to investigate far- and near-field optical properties of plasmonic NPs, especially for a number of important nano-optical applications such as surface-enhanced Raman spectroscopy, photocatalysis, solar cell, and metamaterials.

INTRODUCTRON

Plasmonic nanostructures exhibit unique optical properties mainly due to the quantum confinement effect that would restrict the oscillations of free electrons at nanoscale, therefore resulting in localized surface plasmon resonances (LSPRs) at wavelengths from the ultraviolet to near-infrared (NIR) range. Meanwhile, the electromagnetic field around the plasmonic nanostructures, which are excited by incident light with energies correspond to the LSPR modes, would be greatly enhanced. Applications of nanomaterials with plasmonic characteristics have been explored in tremendous numbers of fields, such as surface-enhanced molecular spectroscopies,[1-4] catalysts,[5-8] photovoltaic,[9-11] optical antenna,[12-14] sensors[15, 16] and so on. More specifically, the enhanced electromagnetic fields around plasmonic nanomaterials play decisive roles in many significant areas like surface-enhanced Raman spectroscopy (SERS)[17-23] and photocatalysis.[24-28] For example, we and Xiao's group recently collaborated on the construction of highly sensitive and photostable gap-enhanced Raman tags (GERTs), with a great amount of strong electromagnetic and chemical hot spots in the interior nanogaps, for intraoperative detection and eradication of residual prostate microtumors, therefore preventing local recurrence and delivering complete tumor-free survival.[17, 20] Liu and coworkers remarkably improved the rate of water splitting with a titanium dioxide substrate coated by gold (Au) nanoparticles (NPs) under visible light irradiation and it was proved that the enhanced electric-fields nearby the water-catalyst interface play major contribution.[28] As fundamental work in practical utilization of plasmonic nanomaterials,

Nanoscale Accepted Manuscript

theoretical guidance on their optical properties is of significant importance. Analytical solution of far-field optical information of plasmonic nanostructures of simple geometries (e.g., sphere and ellipsoid) can be solved readily based on Mie's theory.[29] However, lack of near-field information and disability of solving complex nanostructures limits the wide utilization of analytical method. To overcome the drawbacks of the analytical approach, numerical simulations including the methods of finite-different time domain (FDTD),[30] finite element method (FEM)[31] and discrete dipole approximation (DDA)[32] were developed. By means of these methods, accurate and integrated optical behaviors of plasmonic nanostructures with arbitrary configuration, including far-field optical cross-sections and near-field electromagnetic enhancement, can be harvested, but typically after long-time computation processes. The intrinsic contradiction between the accuracy and the speed of numerical simulation limits the use in fields calling for supports from abundant theoretical models.

Machine learning, as a subset of artificial intelligence, can establish highly complex mapping models for performing a specific task in the data-driven way.[33] It recently develops rapidly and has been applied in various fields like image recognition,[34] disease diagnosis,[35] and strategy making.[36] The associated deep neural network (DNN) imitates the hierarchical structure of brain, where neurons work as the basic data processers and they connect with each other to exchange the information inside.[37] Powerful capability of DNN to encode data enlightens more efficient approaches to acquire various optical characteristics of nanomaterials.[38] Peurifoy and coworkers have used DNNs to establish mappings between the light scattering spectra of multi-shell nanoparticles and their shell thicknesses.[39] Very recent works have successfully demonstrated the correlations between transmission spectra of more complex plasmonic nanostructures and their structural parameters via the DNN training.[40,41] Ma et al.

further combined the reflection and circular dichroism spectra of chiral metamaterials together, to find

deep connection between these optical data and the physical parameters.[42] In addition to more efficient

forward predicting optical responses, researchers also fulfilled the demands of inverse designs to

forecast physical parameters of the optical elements from given far-field properties with utilizing the

merits of DNNs.[39-42] Based on the established mappings, the inverse design model can directly provide

parameters of materials with expected optical characteristics. It skips the repeating simulations in

traditional optimization method to approach the ideal optical properties. Therefore, the on-demand

inverse model significantly improves the efficiency of material design work. However, investigations on

revealing the hidden relevance between the optical properties and dimensional parameters of

nanomaterials via the DNN are still stuck at the range of far-field spectra. The prediction of decisive

near-field optical properties in many applications certainly drew much attention from researchers.

Recently, Barth and Becker attempted the meaningful classification of photonic modes by the DNN

approach, which presents potentials on systemic optimization of nanostructures' electromagnetic

fields.[43] Nevertheless, the lack of exact distributions of near-field information around the nanostructures

limits the practical use of that. Prediction of the vital near-field optical information still remains as a

challenge for the huge space of the electromagnetic field data required.[44]

In this work, we utilized the machine learning method (i.e., DNN) to predict both the far- and near-

field optical properties of three types of plasmonic Au NPs: nanosphere (NS), nanorod (NR), and dimer.

The original far-field absorption, scattering, and extinction spectra and near-field electric-field

enhancements at certain resonance modes calculated from numerical simulations (FDTD in this work)

were used as training datasets for the DNN model. Once the model was trained, the DNN showed highly

accurate prediction on far-field and on-resonance near-field properties compared to the corresponding FDTD simulated results. To the best of our knowledge, it is the first demonstration of successful prediction on the electric-fields enhancement maps around the optical elements through the DNN model, which has long been hindered by the enormous data volume.[44] Ingenious screening and resampling of the electric-field data were carried out to reduce the dimensionality to an acceptable extent for the DNN training. It ought to be noted that in some particular cases, such as the dimers with extremely narrow interparticle gaps, data points containing crucial near-field enhancement information would be lost with the common sampling method. To deal with this issue, a locally-refined sampling approach was employed and thus the accuracy of the predicted near-field enhancement distributions can be greatly improved. Additionally, dimensional parameters of plasmonic NPs can be resolved based on given far-field optical information for the inverse design problem, which largely improves the task efficiency of designing on-demand plasmonic NPs. In contrast to traditional numerical simulations, time and computing resource consumptions of the machine learning method are dramatically decreased. DNN provides a much more efficient solution to gain far- and near-field optical properties of plasmonic nanostructures for the fundamental research and application developments in the fields related to nanooptics.

RESULTS AND DISCUSSION

The far- (e.g., absorption, scattering, and extinction cross-sections) and near-field (e.g., electric-field enhancement distribution) optical properties of plasmonic nanostructures are of great importance and

Nanoscale Accepted Manuscript

are highly dependent on their dimensional parameters such as the particle size and shape. One of the

classical methods to acquire those optical properties of plasmonic nanostructures is the numerical

simulation (Figure 1), where a number of structural and simulation parameters, including the geometry

and dimensions of the object, dielectric data, light source and the polarization direction, the simulation

area, and boundary conditions, have to be set in the simulation model. In this work, we employed the

FDTD method as a typical example to calculate NP's optical properties of interest. The simulating

object and electromagnetic fields are divided into the so-called Yee cells and the Maxwell's equations

can be solved by iteration based on that. However, ideal results require high simulation accuracy in the

FDTD models, which means a large amount of time and computing resource are demanded. Meanwhile,

numerical simulation is a unidirectional pathway to gain the optical information of one nanostructure

with specific dimensions. Therefore, the design of nanostructures with desired optical characters needs

enormous complex simulations to approach the optimization. Herein we propose a much more efficient

bidirectional approach utilizing machine learning (i.e., the DNN model) to predict the far- and near-field

optical properties of the plasmonic nanostructures with the known dimensional parameters. A large

amount of far- and near-field optical data calculated with the FDTD method are used as the training

dataset for the DNN. After the training process, optical properties of the plasmonic nanostructure can be

efficiently predicted. Especially, to the best of our knowledge, this is the first demonstration of

realization of near-field prediction via machine learning method, which overcomes the huge obstacle

caused by enormous data volume. In addition, another significant function, inverse prediction of the

nanostructure's dimensional parameter from its far-field optical data, can also be realized by this

machine learning approach. This is valuable to the inverse design of plasmonic nanostructure with

certain optical properties. With precision of the predictions guaranteed at the same time, the machine

learning provides an ultrafast and computing resource-saving method to the fields concerning about the
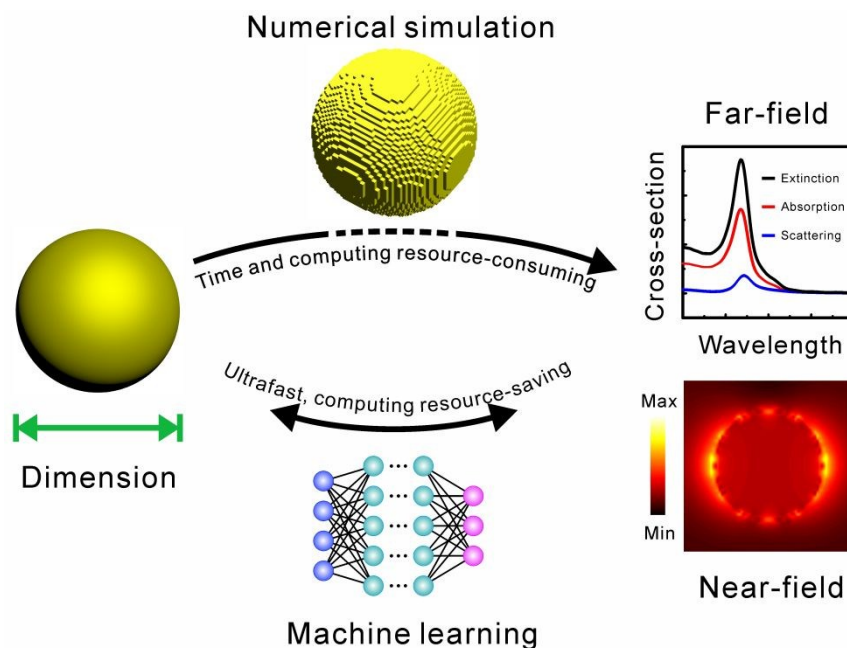
optical properties of plasmonic nanostructures.

Figure 1. Comparison of computational methods for optical simulation of plasmonic nanoparticles (NPs) using numerical simulation and machine learning. The far-field absorption, scattering, and extinction spectra and near-field enhancement ($|E/E_0|$) distribution properties of plasmonic NPs can be predicated using numerical simulation (e.g., finite difference time domain, FDTD) and machine learning (e.g., deep neural network, DNN). The former is time and computing resource-consuming and the latter is highly efficient, ultrafast (< 0.01 s), and computing resource-saving. Furthermore, the physical dimensional parameters of NPs can be predicted via the DNN inversely for an input desired far-field optical response.

The proposed machine learning models for predicting optical properties and designing NPs are shown

in Figure 2a. The training dataset that contains far- and near-field information was obtained by

performing FDTD simulations. There are three machine learning tasks including (i) structure

classification, (ii) spectral DNN for predicting spectra and parameters, and (iii) E-field DNN for

predicting electric-field enhancement, all trained with a number of groups of optical data. Each group

includes the absorption, scattering and extinction spectra, together with a two-dimensional (2D) electric-

field enhancement map at the strongest resonance wavelength of the corresponding NP. Far-field spectra

and structural information were employed to train structure classification model, far-field spectra and

dimensional information to spectral DNN, and electric-field enhancement and dimensional information

to E-field DNN. The trained models can be used to perform forward prediction and/or inverse design for

plasmonic NPs. The structure classification model is only for inverse design task and it typically uses

far-field spectra as input and outputs the structural information. According to the classification result,

the far-field spectra were sent to the DNN of the corresponding NP for the prediction of dimensional

properties. As an auto-encoding neural network which can achieve bidirectional prediction, the spectral

DNN utilizes the given dimensions of the NP as input and predict the far-field spectra during the

decoding process, or allows to obtain a geometry of NP for desired far-field electromagnetic response

during the encoding process (see the details in Methods). The E-field DNN is designed as a generative

neural network only for forward predication of the electric-field enhancement distribution for a

geometry of the NP.

Figure 2b shows the detailed architecture of three machine learning models in Figure 2a. In the

structure classification model (top left), every spectrum was resampled as 57 data points, which mainly

contains information of the peaks. As the input data, three spectra were rearranged into a 1×171 vector.

The dataset contains 3118 groups of optical data including 950 groups for NSs, 1535 groups for NRs,

and 633 groups for dimers. For each nanostructure, 70% of the dataset was used as the training set and

30% as the test set. A DNN model was applied to classify the spectra and determine the corresponding

Nanoscale Accepted Manuscript

NP type. We verified the robustness of this model training process using a 10-fold cross-validation,[45] which divides the training dataset into 10 sub-datasets. One single sub-dataset is reserved for the verification and the other 9 sub-datasets are used for the model training. The average result after 10 times verification was considered as the verification accuracy. In the DNN model, we set the number of trees as 300, and each tree adopts 13 features randomly. Since spectral data is the result of FDTD simulation, there is almost no noise, so verification accuracy and test accuracy are both reached 100%, indicating that the DNN model can effectively classify the NP structure based on the input spectra.
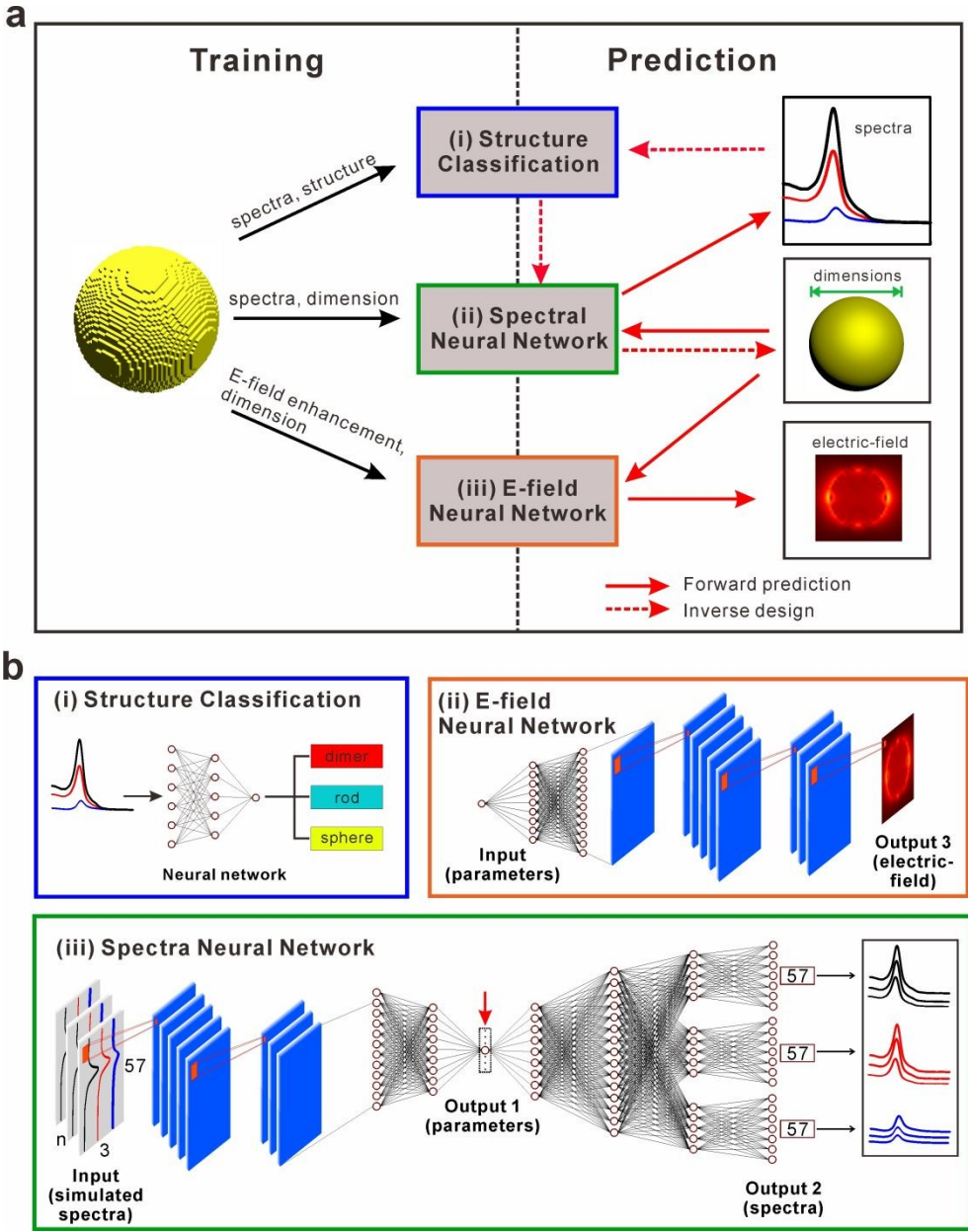
Nanoscale Accepted Manuscript

Figure 2. Structure of machine learning models for optics prediction and designing NPs. (a) Far- and near-field optical data obtained from the FDTD simulations were used to train three different machine learning models: far-field spectra and structural information for (i) structure classification, far-field spectra and dimensions for (ii) spectral DNN, and near-field enhancement maps and dimensions for (iii) E-field DNN. After training, the machine learning models can be used to perform forward prediction and/or inverse design. The solid and dashed red arrows represent the forward predication and the inverse design process, respectively. (b) Detailed architecture of three machine learning models in panel a.

The bidirectional spectral DNN (bottom in Figure 2b) is composed of the forward and reverse parts.

The layers before Output 1 are the inverse purpose, which resolves the mapping from spectra to

1

1

geometrical parameters, and the layers after that are for the forward prediction. For the inverse part, three spectra were combined into an image consisted of 3×57 pixels or multi-spectral prediction. After two traditional convolution layers with max-pooling and flatten layer, the input 3×57 matrix was compressed into a 1×114 vector. After three full-connected layers, the predicted parameters were outputted. The number of neurons in the third full-connected layer (indicated by the red arrow in Figure 2b) is determined by the number of geometrical parameters of NPs, for example, 1 neuron for the NS, 2 for the NR, and 3 for the dimer. In the part for the forward predication training, the followed two full-connected layers with 200 and 500 neurons map the one-dimensional (1D) vector representing the parameters to 1×500 vector. After training three parallel tensor units, which contain two full-connected layers with 200 and 57 neurons, three different spectra with 57 data points were outputted. For single-spectrum prediction, the two convolution layers were replaced by a full-connected layer with 200 neurons and there is only one parallel module in the forward part.

Considering no need of the inverse design based on the given electric-field enhancement information in practice, the unidirectional E-field DNN model (top right in Figure 2b) is designed only for forward electric-field enhancement prediction. In order to make the network converge quickly, each electric-field map is resampled into a smaller image (40×40 pixels for NSs and NRs, 40×80 pixels for dimers). The number of input dimensional parameters of this network is from one to three, while the output layer is an image containing thousands of pixels. With the huge difference between the input and output data dimension, the mismatching degree remarkably increases. Therefore, we introduced the upsampling deconvolution network in the construction of the network, and performed the second training fitting in the strong hot spot areas (e.g., the interparticle gap of the dimer), where the data

Nanoscale Accepted Manuscript

1

2

change dramatically. After passing through the four full-connected layers with 200, 500, 600, and 400

neurons and a reshape layer, the dimensions of data points increased from $1 \times n$ (n = 1, 2, and 3) to $20 \times$

20. The upsampling layer and deconvolution layer were employed to enlarge the data image to 40×40

pixels and the electric-field distribution for NSs and NRs can be obtained. For the dimers, after the extra

upsampling layer and deconvolution layer, the final electric-field enhancement maps with 40×80 pixels

were outputted.
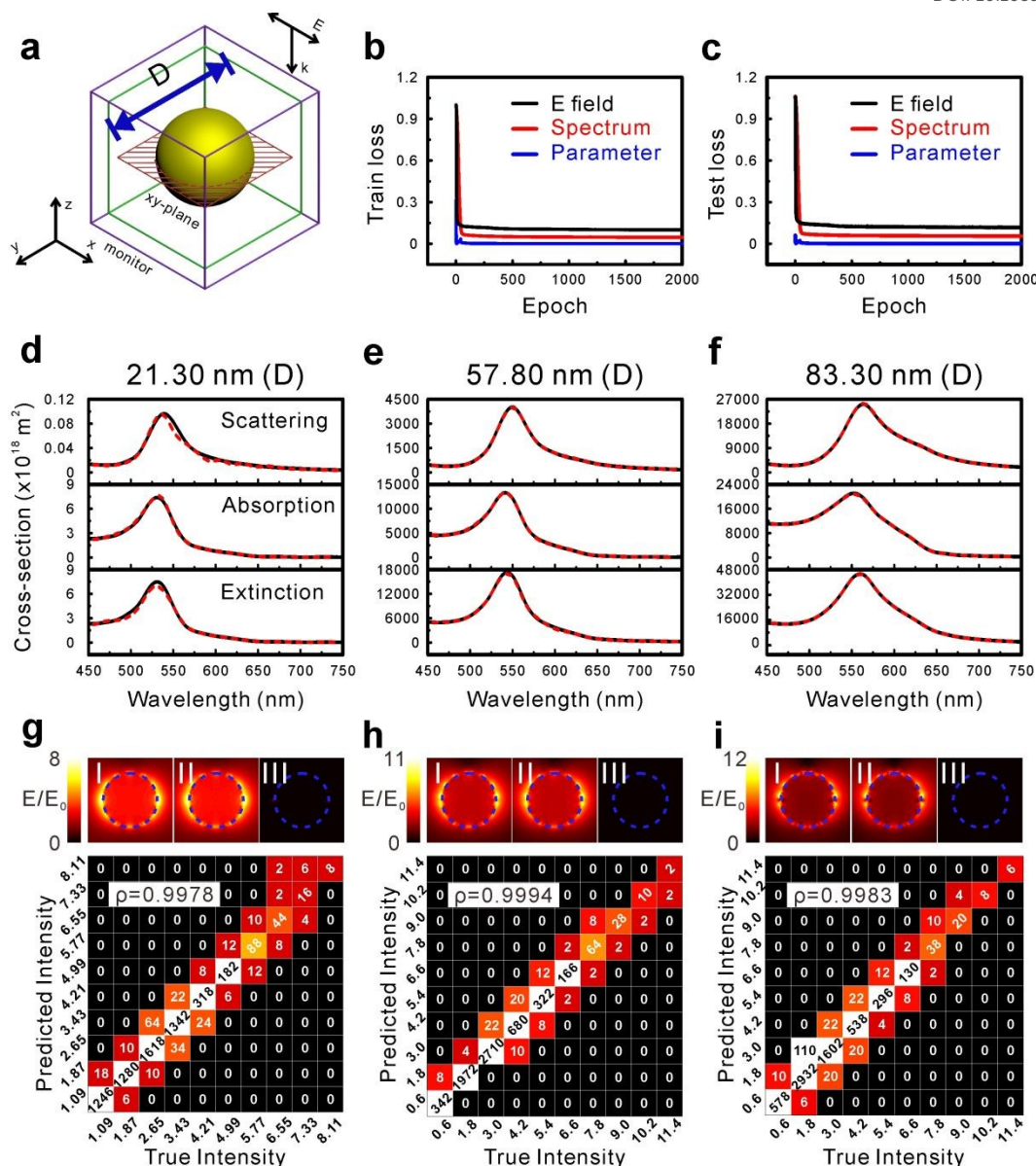
Nanoscale Accepted Manuscript

Figure 3. Prediction of optical properties of a Au nanosphere (NS) through DNN. (a) Schematic of a Au NS (diameter: *D*). The red square represents the *XY*-plane where the electric-field enhancement ($|E/E_0|$) distribution is recorded. The green and purple boxes illustrate the 3D monitors for far-field data. The convergences of predictions of electric-field (black), spectrum (red), and parameter (blue) in (b) training and (c) testing processes. Convergence is defined as the trend of mean square error between the true value and predicted value with the increase of cycle number. Comparisons between FDTD simulated (black solid) and DNN predicted (red dashed) scattering, absorption and extinction spectra (from top to bottom) of a Au NS with a diameter of (d) 21.30, (e) 57.80, and (f) 83.30 nm. (I) FDTD simulated, (II) DNN predicted, and (III) their difference of electric-field enhancement distributions of a Au NS with a diameter of (g) 21.30, (h) 57.80, (i) and 83.30 nm, and their corresponding intensity error maps. The profiles of Au NSs are depicted with blue dashed lines. The Pearson coefficients (ρ) are noted in the maps.

The DNN model was firstly applied to predict optical properties of a Au NS, which is the simplest

plasmonic NP typically with only one dipolar plasmon resonance mode. Figure 3a depicts the model of

a Au NS in the FDTD simulation with a diameter of D in the simulation region. The Au NS is irradiated

by incident light with a propagation (k) along the -Z direction and a polarization (E) along the X

direction. The calculated far-field cross-sections were mainly collected by 3D far-field data monitors

(indicated by green and purple boxes). The near-field electric-field enhancement ($|E/E_0|$) distribution

was collected by a 2D monitor along the XY-plane (indicated by a red shaded square). The far-field

spectra including absorption, scattering, and extinction spectrum of one Au NS with a specific diameter

together with the corresponding on-resonance dipolar electric-field enhancement map are considered as

one group of optical data. Totally 950 groups of optical data of Au NSs with different diameters ranging

from 5 to 100 nm were produced by the FDTD simulation. 70% of them were randomly selected for the

DNN training, and the other 30% data were used as the testing groups to verify the prediction accuracy

from the DNN model later. Figure 3b illustrates the training loss of three variables of interests during

the training process: electric-field enhancement (E field, black), spectral cross-section (spectrum, red)

and diameter (Parameter, blue). The loss represents the root-mean-square-errors (RMSEs, see the details

in Methods) between the practical values and those obtained from the DNN.[46] To further verify this

DNN model, the testing loss curves are presented as well (Figure 3c). Sharp reduction of both training

and testing loss after 60 epochs implies the fast convergence of the model, which suggests strong

reliability of the DNN for prediction. The Au NSs typically show a dipolar LSPR mode in the far-field

spectra,[47] and its wavelength position and intensity greatly determine their potential applications.[48-50] As

examples, Figure 3d-f exhibit the comparison of the FDTD simulated (black solid) and the DNN

predicted (red dashed) scattering, absorption, and extinction spectra (from top to bottom) of Au NSs

with different diameters of 21.30, 57.80 and 83.30 nm. It can be seen that the DNN predicted spectra

perfectly overlap to the FDTD simulated ones in terms of the wavelength position and the intensity of

the dipolar LSPR mode, exhibiting a well-known spectral evolution trend: the LSPR mode redshifts

with the increase of the particle diameter.[51] These results are similar to the previous reports about the

machine learning prediction between the physical parameters of nanophotonic elements and their

corresponding far-field optical spectra.[39-42] However, electric-field enhancements of plasmonic

nanomaterials predicted by the machine learning has not been reported yet to the best of our knowledge,

most likely due to the inability of the DNN model to process such a huge amount of data coming from

simulations.[43, 44] To deal with this difficulty, we came up with a facile dimensionality reduction method

for the original data. Screening and resampling of the electric-field data effectively reduce the volume.

Additionally, only the electric-field enhancement distribution corresponding to the strongest mode (for

NS, it is the dipolar mode) was screened for its representativeness of the crucial maximum electric-field

enhancement ability while others would be ignored. That's to say, the data volume can be reduced to

1/410 of the original size since totally there are 410 sampling points distributed uniformly in the

wavelength range. Next, the resampling process of the screened electric-field data further reduce its

volume. The screened electric-field data performs as a two- dimensional matrix and if each dimension

reduce n times, the resulted volume of the data should be reduced by n^2 times. For example, the area to

record the electric-field data was defined as a square with edge length of 3 times of the diameter and the

mesh size of this area was set as 1/40 of the diameter. Thus, there is a 120×120 matrix and the total

number of data points should be 120^2. The resampling approach decreased each dimension of the

resulted matrix to 40, which means the number of the data points becomes to 40^2 and the resulted

volume of data ought to be reduced to 1/9 of the original screened one. With processes above, the

electric-field data would be appropriate for the DNN training. Figure 3g **I** shows the FDTD simulated

on-resonance (530 nm) dipolar electric-field enhancement map of a Au NS with a diameter of 21.30 nm,

which clearly discloses the dipolar characteristics and a maximum enhancement value up to more than 8.

Interestingly, the corresponding DNN predicted electric-field enhancement map of the dipolar LSPR

mode of a Au NS with the same diameter well reproduce the FDTD simulated one (Figure 3g **II**) in

terms of field intensity and distribution, which can be confirmed by the negligible intensity in the

electric-field enhancement difference map (Figure 3g **III**). To further quantitatively figure out the

discrepancy between the FDTD simulated and the DNN predicted electric-field enhancement, we

employed confusion matrixes analysis of the data pixel by pixel, where the values from the two methods

are compared in each interval of the intensity (bottom in Figure 3g). The Pearson coefficient (ρ), defined

as the extent of linear correlation between two variables, from the confusion matrixes analysis shows a

value of 0.9978, which demonstrates the ultra-high accuracy of the DNN predicted electric-field

enhancement. In addition, the DNN predicted electric-field enhancement maps show ultra-high accuracy

for the dipolar LSPR mode of Au NSs with a diameter of 57.80 and 83.30 nm, proved by the map

comparison and the Pearson coefficient values in Figure 3h and i. These results demonstrate that the

complex and the time-consuming FDTD simulations can be replaced by the machine learning method

(e.g., the DNN model) to obtain Au NSs' far- and near-field optical properties.
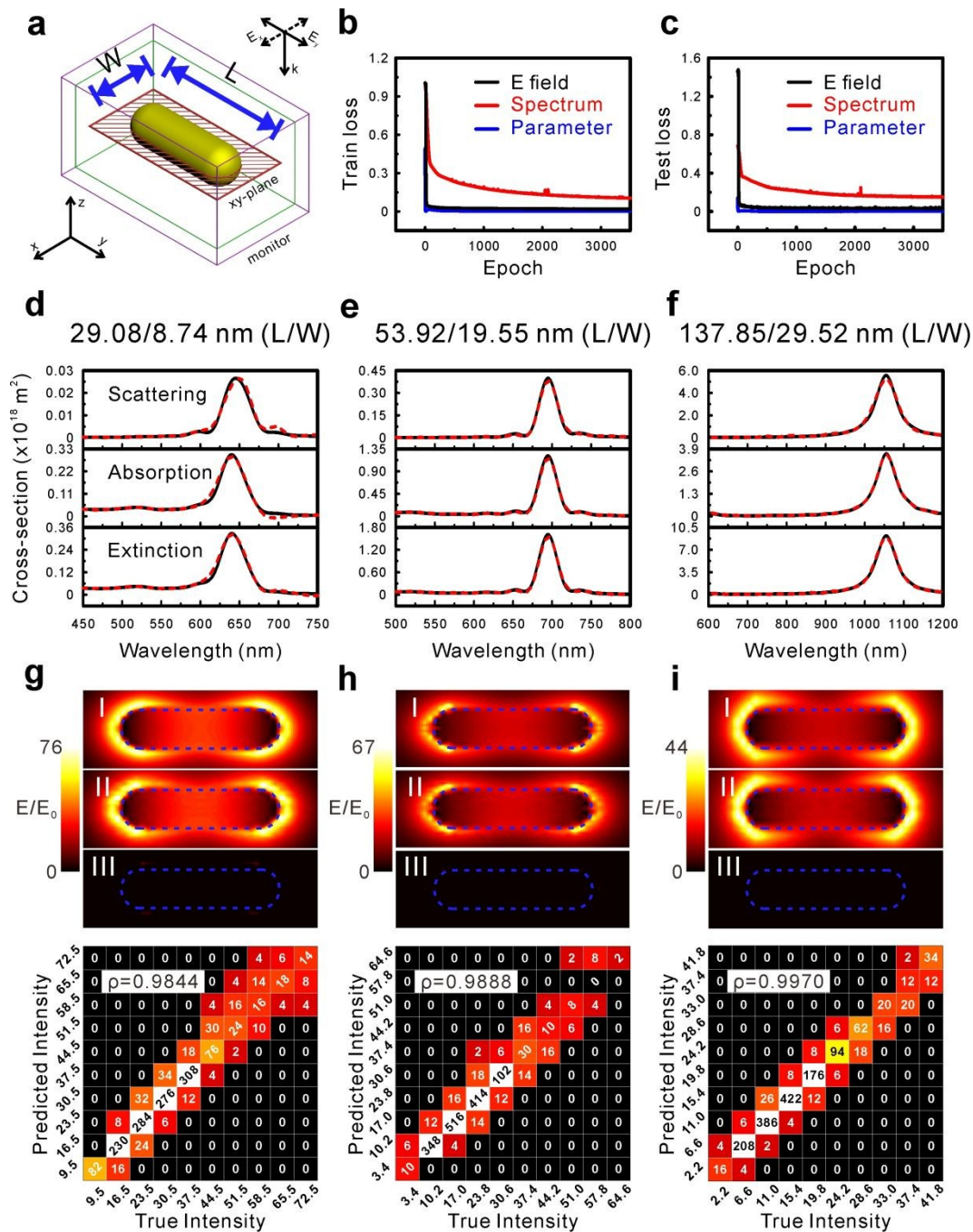
Nanoscale Accepted Manuscript

Figure 4. Prediction of optical properties of a Au nanorod (NR) through DNN. (a) Schematic of a Au NR (length/width: *L/W*). The red rectangle represents the *XY*-plane where the electric-field enhancement distribution is recorded. The green and purple boxes illustrate the 3D monitor for far-field data. Convergences of the predictions of electric-field (black), spectrum (red) and parameter (blue) in (b) training and (c) testing processes. Comparisons between FDTD simulated (black solid) and DNN predicted (red dashed) scattering, absorption and extinction spectra of a Au NR with a dimension (*L/W*) of (d) 29.08/8.74, (e) 53.92/19.55, and (f) 137.85/29.52 nm. (I) FDTD simulated, (II) DNN predicted, and (III) their difference of electric-field enhancement ($|E/E_0|$) distributions of a Au NR with a dimension of (g) 29.08/8.74, (h) 53.92/19.55, and (i) 137.85/29.52 nm, and their corresponding intensity

error maps. The profiles of Au NRs are depicted with blue dashed lines. The Pearson coefficients (ρ) are noted in the maps.

The success to predict far- and near-field optical properties of Au NSs encouraged us to further explore other plasmonic NPs, for example, NRs. Au NRs have been extensively investigated due to their highly tunable plasmon resonances from the visible to NIR range by controlling the dimensional aspect ratio of the longitudinal length and the transversal width.[52] Figure 4a illustrates a Au NR model in the FDTD simulation, with a longitudinal length (L) and a transversal width (W). Incident light propagation direction (k), 3D far-field monitors (green and purple boxes), and the 2D near-field monitor (the red shaded rectangle) are indicated in Figure 4a. The light is polarized parallel to X or Y axis. In total, 1535 groups of optical data (including scattering, absorption, and extinction spectra from two polarizations, and longitudinal dipolar on-resonance electric-field enhancement map) from Au NRs with different aspect ratios were acquired through the FDTD simulations. The length of the Au NRs ranges from 10 to 200 nm and the width is between 1/5 and 1/2 of the length. Similarly, obvious convergence can be found in the DNN training and testing processes using 70% of the optical data for the verification and 30% data for the testing (Figure 4b and c). Figure 4d-f depict simulated (black solid) and predicted (red dashed) scattering, absorption and extinction spectra (top to bottom) of three Au NRs with dimensions (L/W) of 29.08/8.74, 53.92/19/55, and 137.85/29.52 nm. Dual-mode (corresponding to transversal and longitudinal dipolar resonances) characteristics of Au NRs' can be reflected on their far-field spectra from both the FDTD simulation and the DNN prediction, although the intensities of transversal dipolar modes are pretty weak. They both exhibit that the dipolar LSPR mode redshifts with the increase of the aspect ratio between the longitudinal length and the transverse width. More importantly, great fitness

Nanoscale Accepted Manuscript

between the simulated and predicated spectra indicates high accuracy of the DNN predicted far-field

optical properties for Au NRs. As the most representative characteristic of Au NRs, the longitudinal

dipolar on-resonance electric-field enhancement maps are chosen in the DNN training process and for

the comparison between the simulation and predication. Figure 4g-i compare the simulated and

predicted the longitudinal dipolar electric-field enhancement maps of three Au NRs, as indicated in

Figure 4d-f. High similarity between the simulated and predicted electric-field enhancement distribution

(Figure 4g-i, **I** and **II**) and the negligible differences (Figure 4g-i, **III**) show ultra-high accuracy of the

DNN predictions both on the location and intensity of the Au NR's near-field information. Confusion

matrixes examine the errors statistically between the electric-field intensities from two approaches

above (bottom in Figure 4g-i). The true and predicted intensities almost overlap in every interval around

the diagonal line with all Pearson coefficients larger than 0.98, also implying high precision of the DNN

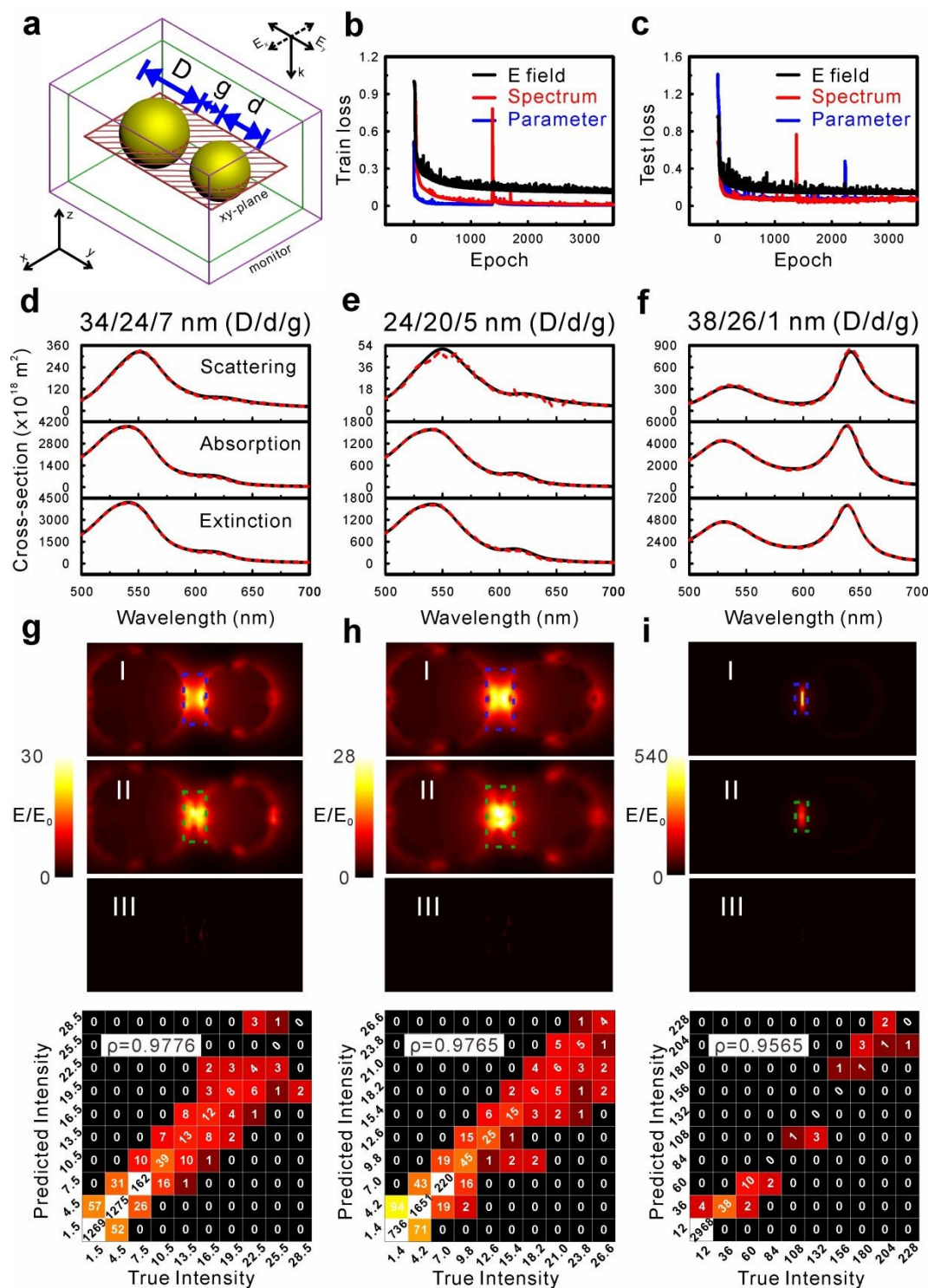prediction on the near-field properties of Au NRs.

Figure 5. Prediction of optical properties of a Au NS dimer by DNN. (a) Schematic of a Au NS dimer (diameter/diameter/inter-particle distance: $D/d/g$). Convergences of the predictions of electric-field (black), spectrum (red) and parameter (blue) in (b) training and (c) testing processes. Comparisons between FDTD simulated (black solid) and DNN predicted (red dashed) scattering, absorption and extinction spectra of Au NS dimers with a dimension of (d) 34/24/7, (e) 24/20/5, and (f) 38/26/1 nm. (I) FDTD simulated, (II) DNN predicted, and (III) their difference of electric-field enhancement ($|E/E_0|$) distributions of Au NS dimers with dimensions of (g) 34/24/7, (h) 24/20/5, and (i) 38/26/1 nm, and their

corresponding intensity error maps. The profiles of Au NRs are depicted with blue dashed lines. The Pearson coefficients (ρ) are noted in the maps.

Compared to the NS and NR, the dimer is a more complex nanostructure with more dimensional parameters including two particle diameters (D and d) and an interparticle distance (g). The far- and near-field optical properties of dimers are strongly dependent on the interparticle distance,[53] and therefore they have been widely investigated for the applications of photothermal convertor[54] and biomolecule sensor.[55] For example, electromagnetic hot spots with an electric-field enhancement factor larger than 43 can be formed in the gap of plasmonic dimers when the interparticle distance is about 3 nm.[56] These electromagnetic hot spots are a crucial factor for molecular enhanced spectroscopy.[57, 58] Therefore, we further explore the DNN model to predict optical properties of plasmonic dimers, especially the electric-field enhancement in the interparticle gap. Figure 5a illustrates a model of a Au dimer (diameter/diameter/inter-particle distance, $D/d/g$) in FDTD simulation. Their particle diameters were controlled between 20 to 40 nm and the interparticle distance was ranged between 1 to 10 nm. Incident light propagation direction (k), 3D far-field monitors (green and purple boxes), and the 2D near-field monitor (the red shaded rectangle) are indicated in the simulation model in Figure 5a. Typical light polarization along to X or Y direction was employed and the final far-filed spectra were averaged on those from two polarizations. Totally, 633 groups of optical data from the simulations were used for the training and testing of the DNN model. Fast convergence during these processes indicates the robustness of the DNN model (Figure 5b and c). Figure 5d-f describe the FDTD simulated (black solid) and the DNN predicted (red dashed) far-field scattering, absorption and extinction spectra (from top to bottom) of Au NS dimers with different dimensional parameters ($D/d/g$): 34/24/7, 24/20/5, and 38/26/1

nm, respectively. Comparison of these spectra reveals good fitness between the FDTD simulations and

the DNN predictions, both showing a trend: the plasmon coupling effect is significantly enhanced with

the shrinkage of the interparticle distance the Au dimers. For example, dipolar plasmon modes of the

individual particle are dominant and only a very weak plasmon coupling mode can be found in the range

of 600-650 nm for the interparticle distances of 7 and 5 nm (Figure 5d and e). However, when the

interparticle distance shrinks to 1 nm, a prominent coupling mode appears at around 640 nm (Figure 5f).

This spectral evolution is very consistent to the previous report by Romero et. al.[53] For the near-field

property training, we selected the mode mainly depending on the wavelength of the strongest resonance

mode on the far-field spectrum. For example, the longitudinal dipolar resonance modes of Au dimers

were selected for the interparticle distance of 7 and 5 nm (**I** in Figure 5g and h), since the electric-field

enhancement at the dipolar modes (both at 542 nm for the dimer of 34/24/7 and 24/20/5 nm) is

dramatically larger than that at the coupling modes based on the FDTD simulations (at 618 nm for the

dimer of 34/24/7 nm and 613 nm for 24/20/5 nm) (see Figure S1 and S2). In contrast, the electric-field

enhancement at the coupling mode was selected for the dimer with an interparticle distance of 1 nm (**I** in

Figure 5i), since it reaches a maximum value beyond 500, much greater than that of the dipolar mode

(Figure S3). After training the DNN model can successfully predict the electric-field enhancement maps

for the dimer of 34/24/7, 24/20/5, and 38/26/1 nm, showing a similar trend that the near-field

enhancement in the gap region turns stronger with the shrinkage of the interparticle distance (**II** in

Figure 5g-i). It can be seen that differences between the FDTD simulated and the DNN predicted

electric-field distributions can be difficultly distinguished (**III** in Figure 5g-i). Further quantitative

comparison of whole electric-field maps by confusion matrixes show that the precision of near-field

Nanoscale Accepted Manuscript

2

3

prediction can be guaranteed with the Pearson coefficients of around 0.98 for the case of a large

interparticle distance (bottom in Figure 5g and h). When the interparticle gap size reduces to 1 nm, the

prediction accuracy obviously decreases and the Pearson coefficient drops to around 0.95 (bottom in

Figure 5i). After careful examination, we also noticed that the near-field discrepancy between the FDTD

simulation and the DNN prediction is mainly contributed by the parts in the interparticle gap regions

(indicated by dashed rectangles in Figure 5g-i), which are also the most important parts for the dimers.

This should be ascribed to the coarse sampling method during the training process of the DNN model,

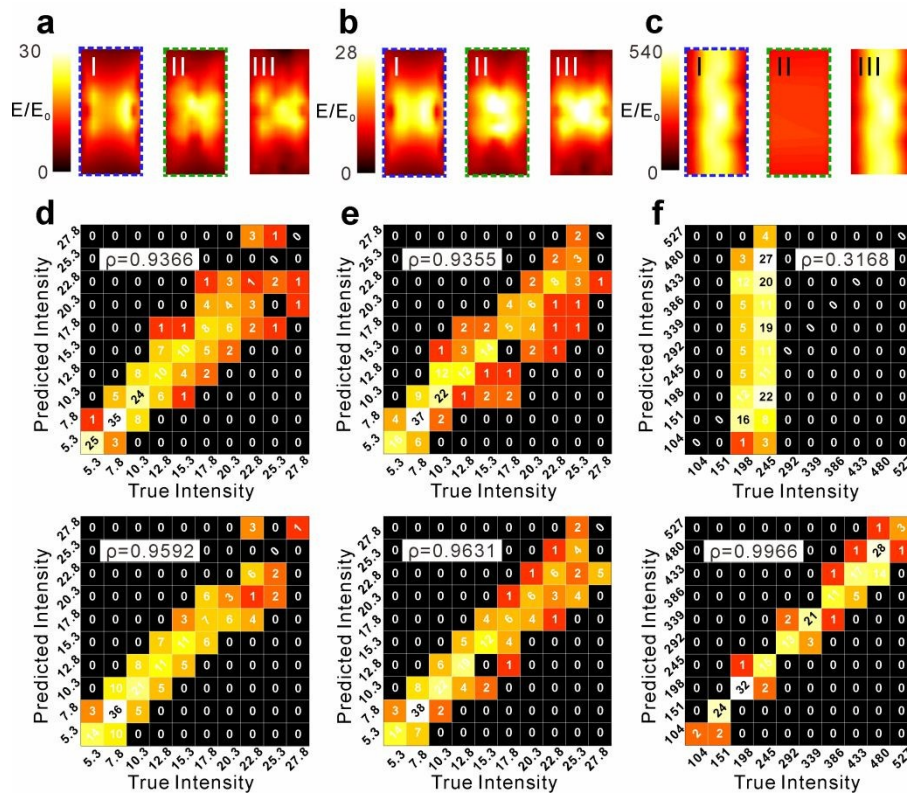which cannot provide a sufficient resolution in such a confined region.

Figure 6. Optimization of electric-field predictions in the gap region of a Au NS dimer by DNN. These gap regions are depicted with blue and green dashed rectangles in Figure 5. (I) The simulated, (II) predicted, and (III) locally-refining predicted electric-field enhancement in the gap region of a Au NS dimer with dimensions ($D/d/g$) of (a) 34/24/7, (b) 24/20/5, and (c) 38/26/1 nm. (Top) Intensity error maps between the FDTD simulated and DNN predicted electric-field enhancements in the gap regions and (bottom) the maps between the FDTD simulated and locally-refining DNN predicted electric-field

enhancements in the gap regions for Au NS dimers with dimensions of (d) 34/24/7, (e) 24/20/5, and (f) 38/26/1 nm.

To solve the problem of losing near-field data in the interparticle gaps of Au dimers, we employed a much-refined sampling approach. Figure 6a-c exhibit the FDTD simulated and the DNN predicted electric-field enhancement maps only in the gaps of Au dimers from Figure 5. It can be noted that the prediction accuracy with the coarse sampling method remarkably decreases when the gap narrows (**I** and **II** in Figure 6a-c). Especially, strong intensity of electric-field in the 1-nm gap is thoroughly ignored by the DNN model (**II** in Figure 6c). The error maps obtained from the confusion matrixes assessment also indicate that the simulated and predicted values basically overlap along with the diagonal line with a wider distribution (the Pearson coefficients maintain above 0.93) for the large interparticle distances (top in Figure 6d-f), but the predicted intensity values no longer correspond to the simulated ones along with the diagonal line and the Pearson coefficient decreases dramatically to 0.3168 for the 1-nm gap size. After applying a locally-refined sampling approach (see the details in Method) that avoids the unacceptable loss of data points recording the electric-field enhancement, precision of those predicted distributions in the gap region is obviously improved, especially for the dimer of 1-nm gap size (see **I** and **III** in Figure 6a-c). For the Au dimers with an interparticle gap of 7 and 5 nm, the refined sampling approach leads to a slightly narrower distribution of the intensity value units around the diagonal line and the Pearson coefficients roughly increase from 0.93 to 0.96 (Figure 6d and e). It should be noted that the Pearson coefficient value greatly increases from 0.3168 to 0.9966 with a rather narrow distribution of the intensity value units along the diagonal line using the finer sampling approach, which

implies that details of electric-field enhancement in the small gap area can be precisely predicted by the
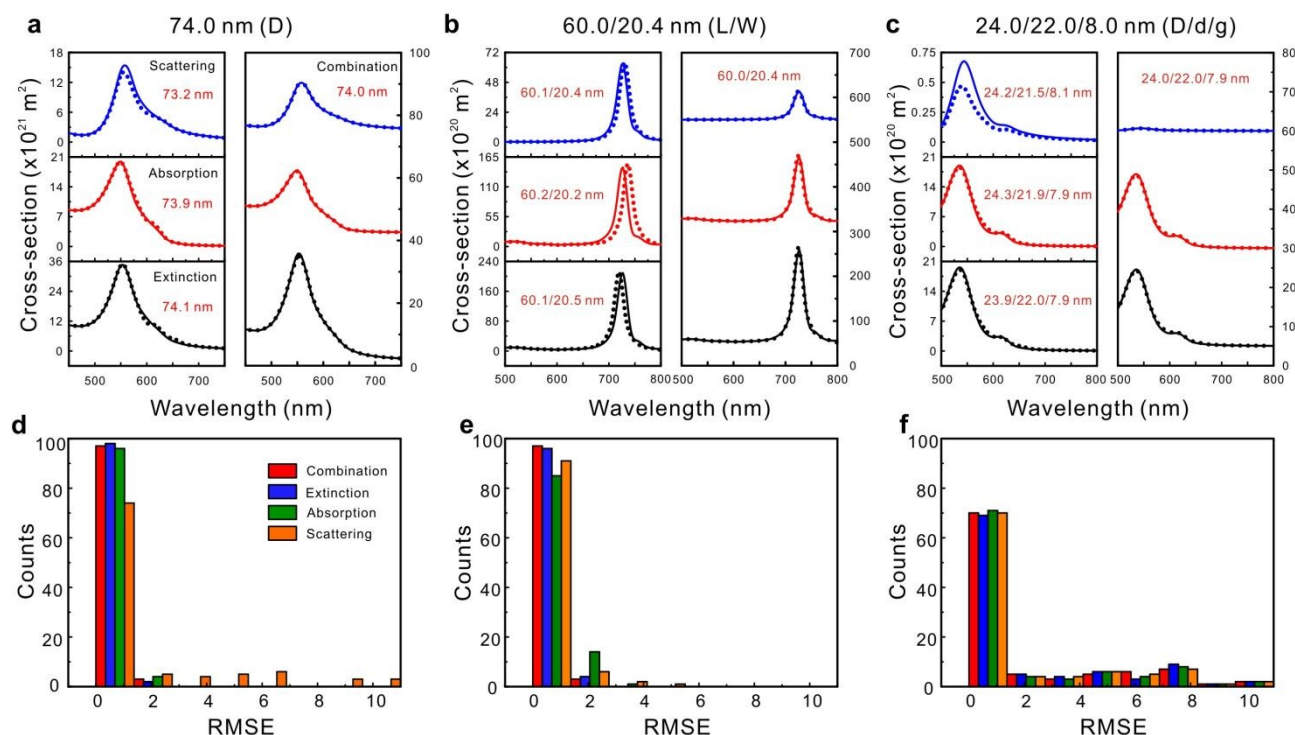
DNN model.

Figure 7. Inverse predictions of physical parameters of NPs from given far-field spectra. Inversely predicted dimensional parameters (marked red) based on given individual far-field scattering (blue), absorption (red), extinction (black) spectrum or their combination for the Au (a) NS, (b) NR, and (c) dimer (see all solid curves). All dashed curves show the corresponding scattering, absorption and extinction spectra by conducting FDTD calculations using the predicted dimensional parameters. (d-f) Quantitive comparison between inversely predicted physical parameters (labeled red in the panels) and the actual ones (labeled black on the top of panels) for the Au (d) NS, (e) NR, and (f) dimer via the root-mean-square-errors (RMSEs).

Design of plasmonic nanostructures with on-demand far-field optical properties, e.g., with strong

absorption in the UV region for plasmonic lithography[59] or with pronounced scattering in the visible

region for dark-field spectroscopy[60], shows great significance in practical applications. However, the

traditional designs have to endure the long processes of repeating the complicated numerical simulations

with different dimensional parameters to optimize the calculated results which meet the requirements of

optical properties. Such tedious inverse optimization tasks often cost long time, especially when high

accuracy of the simulation is demanded. Therefore, it is important to develop a method that efficiently

predicts the dimensional parameters of the nanostructure with given or desired optical information. Very

recently, scientists have reported on various inverse design approaches to predict the structural

dimensions using neuron networks.[39-42] Herein, we also realized highly efficient design of the plasmonic

NS, NR and dimer with desired far-field optical responses through the inverse DNN. The layers

between input layer and first output layer were intercepted as the inverse DNN to design parameters of

NPs according to the given spectra in the spectral DNN. We designed three simple neural networks

whose convolutional layers were replaced by two fully-connected layers to perform single spectrum

prediction. In order to ensure the reliability of the comparison, we employed the auto-encoding neural

network for single spectrum prediction, and used the same optimization method and training epochs.

Individual scattering, absorption, extinction spectrum or their combination corresponding to each

parameter in the dataset were employed to train the neural network. Figure 7a shows a typical example

of inverse design for the Au NS. We used the individual FDTD calculated far-field scattering,

absorption, extinction spectrum or their combination as the given spectral information (see solid curves

in Figure 7a), the predicted diameters (marked red) via the DNN model all are very close to the actual

value 74.0 nm, with a size difference smaller than 1 nm. For comparison between the inversely

predicted parameters and the actual ones more intuitive, we further obtained the scattering, absorption

and extinction spectra by conducting numerical FDTD calculations using the predicted diameters

(dashed curves in Figure 7a), showing a perfect fitting to the given spectra. Similarly, the inverse

prediction works well for the Au NRs and dimers based on the given individual scattering, absorption,

extinction spectrum or their combinations (Figure 7b and c). We summarized 100 cases of quantitative

comparison between inversely predicted physical parameters (labeled red in the panels) and the actual

ones (labeled black on the top of panels) for each type of NP (Figure 7d-f). The distribution diagrams

show that most of RMSE values are smaller than 2 nm, indicating pretty high accuracies of inverse

predictions. We have noticed that the inverse predictions based on the given extinction are more

accurate than that from the scattering and absorption for all three kinds of NPs. Moreover, the

combination of three far-field spectra further improves the prediction accuracy. However, it can be also

found that the prediction accuracy for dimers is relatively poorer in contrast to the NSs and NRs (Figure

7f). This could be possibly explained by the fact that the training data size for dimer is relatively small

compared with the number of parameters, resulting in sparse data distribution. Comparing with NSs and

NRs, dimers has more parameters but the amount of data is almost the same. Neural network is a data-

driven model, which requires a certain amount of data to ensure the fitting effect of the model. The lack

of data volume leads to poor generalization ability of the same neural network model for dimers which

means prediction effect of the model on unknown data is not satisfactory. With more computing

resources, more data can be obtained and the prediction accuracy can be improved. The more

independent identically distributed data that are assigned to the neural network, the stronger the fitting

effect of the model on the data will be, and the better the fitting effect on the unknown data will be.

From the practical point of view, the given far-field optical properties can be obtained from various

approaches including simulations (analytical or numerical) and experimental measurements (e.g., UV-

Vis absorption/transmission measurement or dark-field scattering spectrum measurements). Therefore,

the DNN model can be possibly trained by the experimental dark-field scattering spectrum and the

corresponding actual physical dimensions obtained from scanning electron microscopy (SEM) images at a single plasmonic NP level. This would make both the forward and inverse predictions more of practical significance.

In addition to the prediction accuracy, another merit of the machine learning algorithm is rapidity. We quantitatively compare the calculation time consumed by the FDTD and the DNN method for the Au NSs, NRs, and dimers (Figure S4). To collect far- and near-field optical data mentioned above from the FDTD simulations, totally more than 3000 simulations have been performed on a server (16 cores of AMD Opteron 6376 and 64 GB RAM) and most of them last for $\sim 10^3$ seconds. For the structure with a higher complexity, such as the Au dimer, a number of simulations even last for $10^4 \sim 10^5$ seconds to obtain the final results, especially for those with an interparticle distance smaller than 2 nm (Figure S4c). In contrast, the average time (t_{NN}) consumed by the DNN prediction of the near-field information, performed on a laptop (2 cores of Intel i5-4200M and 8 GB RAM), is only about 10^{-3} seconds, once the training process is accomplished. The huge difference of computing time between these two approaches reaches to more than 6 orders of magnitude. Therefore, we demonstrate that the DNN is an ultrafast, highly efficient, and computing resource-saving approach to predict the far- and near-field optical properties of plasmonic nanostructures.

CONCLUSIONS

Nanoscale Accepted Manuscript

In summary, we succeeded in establishing DNN models to forecast the far-field and near-field optical properties of plasmonic Au NS, NR, and dimer, after using more than 2000 FDTD optical simulations as the train dataset. The DNN models can accurately predict the absorption, scattering and extinction cross-section with input dimensional parameters of those NPs. More importantly, it for the first time realizes the precise prediction of two-dimensional on-resonance electromagnetic enhancement around the NPs with Pearson coefficients larger than 95% compared to the FDTD simulations. We overcame the difficulty produced by the huge volume of the electric-field data generated by FDTD simulations with screening and resampling methods and only selecting the most interesting on-resonant electric-field data. This effectively reduces the volume of electric-field data by at least three thousand folds to an appropriate extent for the DNN training. Moreover, precise predication of the electromagnetic hot spots (e.g., from the interparticle region) can also be confirmed by employing a locally-refined sampling approach. These predictions by DNN were realized typically in less than 10^{-2} second on a laptop, which is 6 orders faster than typical numerical simulations implemented on a server. Finally, we demonstrated that an intelligent inverse design of plasmonic NPs with on-demand optical characteristic can also be fulfilled with the merit of the DNN model. We believe that the DNN can become ultrafast, highly efficient, and computing resource-saving tool to investigate plasmonic properties for fundamental researches and plasmon-relevant applications. It can be further prospected that the DNN model combined with experimental data can be developed in the near future and will lead to a new revolution in the nanophotonic field.

METHODS

Numerical simulation. The numerical far-field absorption, scattering, and extinction spectra and near-field electromagnetic enhancement distribution were calculated by employing the FDTD method using commercial software FDTD Solutions (Lumerical. Inc.). All calculations are performed with a total-field scattering-field (TFSF) source. Empirical optical dielectric data of Au (CRC)[61] was fitted with the Lumerical's multi-coefficient model (MCM)[62] during the calculations of Au NPs. The surrounding refractive index of the models was set as 1.33 to mimic aqueous environment. For the asymmetric Au NRs and NS dimers, their far-field spectra of were acquired by averaging the results from individual simulations with mutually perpendicular polarizations of light source, for the reason that more than one light polarization should be considered. The wavelength range of far-field monitor was set as 400 to 1400 nm to cover the LSPR peaks of the three types of nanostructures and 410 sampling points were distributed uniformly in this range. An additional refined mesh region was added to override the whole object model. To ensure the accuracy of the simulations and avoid the unnecessary cost of time, the smallest mesh size in the simulation region was adjusted flexibly. Specifically, it was set as one third of the length of each nanostructure's smallest dimension (e.g., the gap length of the Au NS dimers). However, it should be controlled less than 5 nm when the smallest dimension went larger than 15 nm.

Machine Learning. An auto-encoding neural network was designed as a bidirectional deep neural network (DNN) to perform spectral prediction and dimensional parameters prediction.[40] The DNN model has one input layer and two output layers corresponding to the ends of the encoder and the decoder, respectively (see Figure 2). The input is a dataset composed of multiple images. Each image that consists of 3×57 pixels was a combination of three spectra containing 57 data points. The

number of neurons in bottleneck layer (first output layer) where all input information is condensed to

minimum is equal to the number of nanostructure parameters (1 neuron for nanosphere, 2 neurons for

nanorod, or 3 neurons for dimer). The penultimate layer was split into three branches so that the final

layer, as the second output layer, would output three spectra through three parts with 57 neurons each.

The network structure before and after the first output layer constitutes the model of inverse prediction

parameters and forward prediction spectra, respectively, which were defined as the encoding and

decoding process. For the inverse network, two convolutional layers followed by two full-connected

layers were employed. For the forward network, four convolution layers are used to map several

neurons to three spectra. The RMSE serves as the assessment of the DNN's accuracy and it is defined as

$$\text{RMSE} = \sqrt{\frac{1}{n}\sum_{i=0}^{n}(Prac_i - NN_i)^2}$$

Where n is the number of parameters, $Prac_i$ is the value of the **i**th practical physical parameter, and NN_i

is the value of the **i**th parameter obtained from the DNN.

For the electric-field prediction, the designed neural network electric-field is used for forward

prediction as a generative neural network. The large data volume of electric-field enhancement maps

acquired from the FDTD simulations leads to consumption of long time and too many computing

resources during the training process. In this study, two approaches were used to reduce the volume of

the data. First, only the electric-field enhancement at the wavelength corresponding to the strongest

resonance mode on the spectra is screened, so that the number of electric-field enhancement recorded by

the sampling points was reduced from 410 to 1. Second, each electric-field enhancement map is

resampled to reduce the volume of data without losing important information, consequently accelerating

the training speed of neural network. If the number of sampling points in each dimension is reduced to 1

/n , the final size of data will be reduced to $1/n^2$. The reduction of data volume means that on the

premise of ensuring the accuracy of model fitting, each convolution layer can adopt fewer convolution

kernels, thus greatly reducing the computational time and resources. For NSs, with the center as the

origin, the horizontal and vertical data are both sampled at equal intervals between -0.975 and 0.975

times of the diameter. For NRs and dimers, the horizontal data was sampled at equal intervals between -

1.125 and 1.125 times of longitudinal length (for NRs) or the diameter of larger sphere (for dimers),

while the vertical data was sampled between -0.585 and 0.585 times of longitudinal length (for NRs) or

the diameter of larger sphere (for dimers). The map was resampled to 40 $\times$ 40 data points for NSs and

NRs, and 80 $\times$ 40 data points for dimers. However, it is also noticed that the evolution of electric-

field enhancement in the gap area (electric "hot spots" are often the most important sites for

nanophotonics) is too drastic for dimers, leading to poor prediction results. Therefore, we conducted a

locally-refined resampling method for hot spot regions (indicated by white dashed boxes in Figure 5 g-

h), where the horizontal data was sampled at equal intervals between -1.35 and 1.35 times of the

interparticle distance and the vertical data was sampled between -0.585 and 0.585 times of the

interparticle distance. The hot spot regions were then resampled to 40 $\times$ 20 data points and trained by

same DNN architecture. The input parameters units were pre-trained by two full-connected layers which

map the original data to a 1 $\times$ 400 vector. Then the vector was reshaped to a 20 $\times$ 20 vector and fed

into three upsampling convolution layers. The tensor size of the output layer is determined by the

electric-field map of the nanostructure (40 $\times$ 40 for NS and NR or 40 $\times$ 80 for dimer).

3

3

It is a great demand that the structure and parameter information of NPs can be obtained directly and simultaneously according to a given spectrum in practical applications. The neural networks mentioned above can only predict one type of nanostructures and it is impossible to unify the nanostructures with different parameters into a one-dimensional input vector. Therefore, another deep neural network (DNN), which is unexcelled in accuracy among current algorithms, was employed to classify the spectra of different nanostructures and provide necessary information to the network. The DNN model only has two hidden layers which have 300 and 50 neurons separately. The spectra of three different nanostructures were mixed to train the NN model, and the model was used to predict nanostructure by data that had not been trained. According to the results of DNN classification, the spectra are fed into the DNN model of the corresponding nanostructure for parameter prediction.

SUPPORTING INFORMATION AVAILABLE: Additional information is available free of charge in the Internet at http://pubs.acs.org.

3

4

REFERENCES AND NOTES

1. Aioub, M.; El-Sayed, M. A., A real-time surface enhanced raman spectroscopy study of plasmonic photothermal cell death using targeted gold nanoparticles. *Journal of the American Chemical Society* **2016,** *138* (4), 1258-1264.

2. Matricardi, C.; Hanske, C.; Garcia-Pomar, J. L.; Langer, J.; Mihi, A.; Liz-Marzan, L. M., Gold Nanoparticle Plasmonic Superlattices as Surface-Enhanced Raman Spectroscopy Substrates. *ACS nano* **2018,** *12* (8), 8531-8539.

3. Fu, Y.; Zhang, J.; Lakowicz, J. R., Plasmon-enhanced fluorescence from single fluorophores end-linked to gold nanorods. *Journal of the American Chemical Society* **2010,** *132* (16), 5540-5541.

4. Ding, S.-Y.; You, E.-M.; Tian, Z.-Q.; Moskovits, M., Electromagnetic theories of surface-enhanced Raman spectroscopy. *Chemical Society Reviews* **2017,** *46* (13), 4042-4076.

5. Chen, Y.-Z.; Wang, Z. U.; Wang, H.; Lu, J.; Yu, S.-H.; Jiang, H.-L., Singlet Oxygen-Engaged Selective Photo-Oxidation over Pt Nanocrystals/Porphyrinic MOF: The Roles of Photothermal Effect and Pt Electronic State. *Journal of the American Chemical Society* **2017,** *139* (5), 2035-2044.

6. Li, H.; Qin, F.; Yang, Z.; Cui, X.; Wang, J.; Zhang, L., New Reaction Pathway Induced by Plasmon for Selective Benzyl Alcohol Oxidation on BiOCl Possessing Oxygen Vacancies. *Journal of the American Chemical Society* **2017,** *139* (9), 3513-3521.

7.   An, C.; Peng, S.; Sun, Y., Facile synthesis of sunlight‐driven AgCl: Ag plasmonic nanophotocatalyst. *Advanced Materials* **2010,** *22* (23), 2570-2574.

8.   Shi, F.; He, J.; Zhang, B.; Peng, J.; Ma, Y.; Chen, W.; Li, F.; Qin, Y.; Liu, Y.; Shang, W., Plasmonic Enhanced Oxygen Reduction Reaction of Silver/Graphene Electrocatalysts. *Nano letters* **2019.**

9.   Brown, M. D.; Suteewong, T.; Kumar, R. S. S.; D'Innocenzo, V.; Petrozza, A.; Lee, M. M.; Wiesner, U.; Snaith, H. J., Plasmonic dye-sensitized solar cells using core− shell metal− insulator nanoparticles. *Nano letters* **2010,** *11* (2), 438-445.

10.   Gan, Q.; Bartoli, F. J.; Kafafi, Z. H., Plasmonic‐enhanced organic photovoltaics: Breaking the 10% efficiency barrier. *Advanced materials* **2013,** *25* (17), 2385-2396.

11.   Atwater, H. A.; Polman, A., Plasmonics for improved photovoltaic devices. *Nature Materials* **2010,** *9* (3), 205-213.

12.   Jornet, J. M.; Akyildiz, I. F., Graphene-based plasmonic nano-antenna for terahertz band communication in nanonetworks. *IEEE Journal on selected areas in communications* **2013,** *31* (12), 685-694.

13.   Knight, M. W.; Sobhani, H.; Nordlander, P.; Halas, N. J., Photodetection with active optical antennas. *Science* **2011,** *332* (6030), 702-704.

14.   Kinkhabwala, A.; Yu, Z.; Fan, S.; Avlasevich, Y.; Muellen, K.; Moerner, W. E., Large single-molecule fluorescence enhancements produced by a bowtie nanoantenna. *Nature Photonics* **2009,** *3* (11), 654-657.

15.　　Li, J.; Jian, Y.; Chang, C.; Hermans, L.; Dorpe, P. V., Biosensing Using Diffractively Coupled Plasmonic Crystals: the Figure of Merit Revisited. *Advanced Optical Materials* **2014,** *3* (2), 176-181.

16.　　Acimovic, S. S.; Kreuzer, M. P.; González, M. U.; Quidant, R., Plasmon near-field coupling in metal dimers as a step toward single-molecule sensing. *ACS nano* **2009,** *3* (5), 1231-1237.

17.　　Xu, L.; Yan, W.; Ma, W.; Kuang, H.; Wu, X.; Liu, L.; Zhao, Y.; Wang, L.; Xu, C., SERS encoded silver pyramids for attomolar detection of multiplexed disease biomarkers. *Advanced Materials* **2015,** *27* (10), 1706-1711.

18.　　Zhang, Y.; Qiu, Y.; Lin, L.; Gu, H.; Xiao, Z.; Ye, J., Ultraphotostable Mesoporous Silica-Coated Gap-Enhanced Raman Tags (GERTs) for High-Speed Bioimaging. *Acs Applied Materials & Interfaces* **2017,** *9* (4), 3995-4005.

19.　　Bao, Z.; Zhang, Y.; Tan, Z.; Yin, X.; Di, W.; Ye, J., Gap-enhanced Raman tags for high-contrast sentinel lymph node imaging. *Biomaterials* **2018,** *163*, 105-115.

20.　　Qiu, Y.; Zhang, Y.; Li, M.; Chen, G.; Fan, C.; Cui, K.; Wan, J.-B.; Han, A.; Ye, J.; Xiao, Z., Intraoperative Detection and Eradication of Residual Microtumors with Gap-Enhanced Raman Tags. *Acs Nano* **2018,** *12* (8), 7974-7985.

21.　　Jiang, X.; Tan, Z.; Lin, L.; He, J.; He, C.; Thackray, B. D.; Zhang, Y.; Ye, J., Surface-Enhanced Raman Nanoprobes with Embedded Standards for Quantitative Cholesterol Detection. *Small Methods* **2018,** *2* (11).

22.   Jin, X.; He, J.; Ye, J., Nanotriangle-based gap-enhanced Raman tags for bioimaging and photothermal therapy. *Journal of Applied Physics* **2019,** *125* (7).

23.   Zhang, Y. Q.; Liu, Z. Y.; Thackray, B. D.; Bao, Z. Z.; Yin, X.; Shi, F. L.; Wu, J. B.; Ye, J.; Di, W., Intraoperative Raman-Guided Chemo-Photothermal Synergistic Therapy of Advanced Disseminated Ovarian Cancers. *Small* **2018,** *14* (31).

24.   Hou, W.; Hung, W. H.; Pavaskar, P.; Goeppert, A.; Aykol, M.; Cronin, S. B., Photocatalytic Conversion of CO2 to Hydrocarbon Fuels via Plasmon-Enhanced Absorption and Metallic Interband Transitions. *Acs Catalysis* **2011,** *1* (8), 929-936.

25.   Seh, Z. W.; Liu, S.; Low, M.; Zhang, S.-Y.; Liu, Z.; Mlayah, A.; Han, M.-Y., Janus Au-TiO2 Photocatalysts with Strong Localization of Plasmonic Near-Fields for Efficient Visible-Light Hydrogen Generation. *Advanced Materials* **2012,** *24* (17), 2310-2314.

26.   Awazu, K.; Fujimaki, M.; Rockstuhl, C.; Tominaga, J.; Murakami, H.; Ohki, Y.; Yoshida, N.; Watanabe, T., A plasmonic photocatalyst consisting of sliver nanoparticles embedded in titanium dioxide. *Journal of the American Chemical Society* **2008,** *130* (5), 1676-1680.

27.   Linic, S.; Christopher, P.; Ingram, D. B., Plasmonic-metal nanostructures for efficient conversion of solar to chemical energy. *Nature Materials* **2011,** *10* (12), 911-921.

28.   Liu, Z.; Hou, W.; Pavaskar, P.; Aykol, M.; Cronin, S. B., Plasmon resonant enhancement of photocatalytic water splitting under visible illumination. *Nano letters* **2011,** *11* (3), 1111-1116.

29.   Mie, G., Articles on the optical characteristics of turbid tubes, especially colloidal metal

solutions. *Ann. Phys* **1908,** *25* (3), 377-445.

30.   Yee, K., Numerical solution of initial boundary value problems involving Maxwell's

equations in isotropic media. *IEEE Transactions on antennas and propagation* **1966,** *14* (3),

302-307.

31.   Jin, J.-M., *The finite element method in electromagnetics*. John Wiley & Sons: 2015.

32.   Yang, W. H.; Schatz, G. C.; Van Duyne, R. P., Discrete dipole approximation for

calculating extinction and Raman intensities for small particles with arbitrary shapes. *The

Journal of chemical physics* **1995,** *103* (3), 869-875.

33.   Jordan, M. I.; Mitchell, T. M., Machine learning: Trends, perspectives, and prospects.

Science **2015,** *349* (6245), 255-260.

34.   Lopes, A. T.; de Aguiar, E.; De Souza, A. F.; Oliveira-Santos, T., Facial expression

recognition with convolutional neural networks: coping with few data and the training sample

order. *Pattern Recognition* **2017,** *61*, 610-628.

35.   Capper, D.; Jones, D. T.; Sill, M.; Hovestadt, V.; Schrimpf, D.; Sturm, D.; Koelsche,

C.; Sahm, F.; Chavez, L.; Reuss, D. E., DNA methylation-based classification of central

nervous system tumours. *Nature* **2018,** *555* (7697), 469.

36.   Silver, D.; Huang, A.; Maddison, C. J.; Guez, A.; Sifre, L.; Van Den Driessche, G.;

Schrittwieser, J.; Antonoglou, I.; Panneershelvam, V.; Lanctot, M., Mastering the game of Go

with deep neural networks and tree search. *nature* **2016,** *529* (7587), 484.

Nanoscale Accepted Manuscript

37.   Svozil, D.; Kvasnicka, V.; Pospichal, J., Introduction to multi-layer feed-forward neural networks. *Chemometrics and intelligent laboratory systems* **1997,** *39* (1), 43-62.

38.   LeCun, Y.; Bengio, Y.; Hinton, G., Deep learning. *nature* **2015,** *521* (7553), 436.

39.   Peurifoy, J.; Shen, Y.; Jing, L.; Yang, Y.; Cano-Renteria, F.; DeLacy, B. G.; Joannopoulos, J. D.; Tegmark, M.; Soljačić, M., Nanophotonic particle simulation and inverse design using artificial neural networks. *Science advances* **2018,** *4* (6), eaar4206.

40.   Liu, D.; Tan, Y.; Khoram, E.; Yu, Z., Training Deep Neural Networks for the Inverse Design of Nanophotonic Structures. *ACS Photonics* **2018,** *5* (4), 1365-1369.

41.   Malkiel, I.; Mrejen, M.; Nagler, A.; Arieli, U.; Wolf, L.; Suchowski, H., Plasmonic nanostructure design and characterization via Deep Learning. *Light: Science & Applications* **2018,** *7* (1), 60.

42.   Ma, W.; Cheng, F.; Liu, Y., Deep-learning-enabled on-demand design of chiral metamaterials. *ACS nano* **2018,** *12* (6), 6326-6334.

43.   Barth, C.; Becker, C., Machine learning classification for field distributions of photonic modes. *Communications Physics* **2018,** *1* (1), 58.

44.   Yao, K.; Unni, R.; Zheng, Y., Intelligent nanophotonics: merging photonics and artificial intelligence at the nanoscale. *Nanophotonics* **2018**.

45.   Wong, T.-T., Performance evaluation of classification algorithms by k-fold and leave-one-out cross validation. *Pattern Recognition* **2015,** *48* (9), 2839-2846.

46.   Ghaedi, M.; Asfaram, A.; Mazaheri, H., Application of machine/statistical learning, artificial intelligence and statistical experimental design for the modeling and optimization of

methylene blue and Cd(II) removal from a binary aqueous solution by natural walnut carbon.

PCCP (Physical chemistry chemical physics) **2017,** *19* (18), 11299-11317.

47.   Kelly, K. L.; Coronado, E.; Zhao, L. L.; Schatz, G. C., The optical properties of metal

nanoparticles: the influence of size, shape, and dielectric environment. ACS Publications:

2003.

48.   Li, Z.; Huang, H.; Tang, S.; Li, Y.; Yu, X.-F.; Wang, H.; Li, P.; Sun, Z.; Zhang, H.;

Liu, C., Small gold nanorods laden macrophages for enhanced tumor coverage in

photothermal therapy. *Biomaterials* **2016,** *74*, 144-154.

49.   Linic, S.; Aslam, U.; Boerigter, C.; Morabito, M., Photochemical transformations on

plasmonic metal nanoparticles. *Nature materials* **2015,** *14* (6), 567.

50.   Rycenga, M.; Cobley, C. M.; Zeng, J.; Li, W.; Moran, C. H.; Zhang, Q.; Qin, D.; Xia,

Y., Controlling the synthesis and assembly of silver nanostructures for plasmonic applications.

Chemical reviews **2011,** *111* (6), 3669-3712.

51.   Steinigeweg, D.; Schütz, M.; Salehi, M.; Schlücker, S., Fast and cost‐effective

purification of gold nanoparticles in the 20‐250 nm size range by continuous density gradient

centrifugation. *Small* **2011,** *7* (17), 2443-2448.

52.   Shao, L.; Li, Q.; Wang, J.; Chen, H., Gold nanorods and their plasmonic properties.

Chemical Society reviews **2013,** *42* (7), 2679-2724.

53.   Aizpurua, J.; Bryant, G.; Romero, I., Plasmons in nearly touching metallic

nanoparticles: singular response in the limit of touching dimers. *Optics express* **2006,** *14* (21),

9988-9999.

54.   Baffou, G.; Quidant, R.; García de Abajo, F. J., Nanoscale control of optical heating in complex plasmonic systems. *ACS Nano* **2010,** *4* (2), 709-716.

55.   Gonzalez, M.; Aćimović, S.; Kreuzer, M.; González, M.; Quidant, R., Plasmon near-field coupling in metal dimers as a step toward single-molecule sensing. *ACS Nano* **2009,** *3* (5), 1231-1237.

56.   Talley, C.; Jackson, J.; Oubre, C.; Grady, N.; Hollars, C.; Lane, S.; Huser, T.; Nordlander, P.; Halas, N., Surface-enhanced Raman scattering from individual au nanoparticles and nanoparticle dimer substrates. *Nano Letters* **2005,** *5* (8), 1569-1574.

57.   Aizpurua, J.; Kall, M.; Apell, P.; Xu, H. X., Electromagnetic contributions to single-molecule sensitivity in surface-enhanced Raman scattering. *Physical Review E: Statistical Physics, Plasmas, Fluids, and Related Interdisciplinary Topics* **2000,** *62* (3), 4318-4324.

58.   Gresillon, S.; Fort, E., Surface enhanced fluorescence. *Journal of physics. D. Applied physics* **2008,** *41* (1), 013001.

59.   Srituravanich, W.; Fang, N.; Sun, C.; Luo, Q.; Zhang, X., Plasmonic nanolithography. *Nano letters* **2004,** *4* (6), 1085-1088.

60.   Jiang, L.; Yin, T.; Dong, Z.; Liao, M.; Tan, S. J.; Goh, X. M.; Allioux, D.; Hu, H.; Li, X.; Yang, J. K., Accurate modeling of dark-field scattering spectra of plasmonic nanostructures. *ACS nano* **2015,** *9* (10), 10039-10046.

61.   Haynes, W. M., *CRC handbook of chemistry and physics*. CRC press: 2014.

62.   Lumerical. https://www.lumerical.com/products/fdtd-solutions/.

TOC